



Die Grenzen der
Chemie neu ausloten?
It takes
#HumanChemistry

Wir suchen kreative Chemikerinnen und Chemiker,
die mit uns gemeinsam neue Wege gehen wollen –
mit Fachwissen, Unternehmertum und Kreativität für
innovative Lösungen. Informieren Sie sich unter:

evonik.de/karriere

The Effect of Chemistry and 3D Microstructural Architecture on Corrosion of Biodegradable Mg–Ca–Zn Alloys

Daniela Zander,* Paul Zaslansky, Naemi A. Zumdick, Markus Felten, Christian Schnatterer, Veronika F. Chaineux, Jörg U. Hammel, Malte Storm, Fabian Wilde, and Claudia Fleck

The development of biodegradable Mg–Ca–Zn alloys strongly relies on the understanding of the varying 3D microstructural architectures by means of high-density-resolution imaging, such as synchrotron radiation-based X-ray microtomography (SR- μ CT). The development of useful strategies to control the degradation process, including the design of appropriate 3D microstructures, focusing on the type, fraction, morphology, distribution, connectivity, and interfaces of different phases, depends on a comprehensive understanding of the underlying corrosion processes. SR- μ CT enables the nondestructive analysis of the same microstructure within a volume exposed to different immersion times in artificial physiological solutions, e.g., Hanks' balanced salt solution without glucose (HBSS). In this work, quantitative 3D imaging via SR- μ CT demonstrates the formation of a continuous 3D network of secondary phases for low-alloyed Mg–Ca–Zn. Furthermore, a change in the corrosion mechanism from very localized to uniform heterogeneous corrosion processes is observed. This mechanistic change is associated not exclusively with the electrochemical activity of the primary α -Mg_{SS} and the secondary (Mg,Zn)₂Ca and Mg–Ca–Zn phases, but also with their volume fraction, distribution, 3D morphology, connectivity, and the formation of corrosion product layers.

Among other magnesium alloys,^[1–4] Mg–Ca–Zn alloys combine a number of advantageous properties, such as biocompatibility,^[5,6] bone-like density, and appropriate mechanical strength.^[7,8] Spontaneous dissolution of magnesium and its alloys based on biocompatible alloying elements in aqueous media is believed to facilitate biodegradation and stimulate bone regeneration.^[9,10]

With increasing popularity of these alloys, questions regarding controllable degradation rates during medium and long-term exposure to corrosive biological media have emerged. Furthermore, there is a particular need for improved strategies to the weak mechanical integrity observed prior to complete bone healing.^[11,12] This has led to extensive efforts in the development and design of biodegradable Mg–Ca–Zn alloys. Low-alloyed Mg–Ca–Zn alloys have come into scientific focus as their degradation process and mechanical properties can be adjusted by varying the alloy composition and optimizing the processing routes through casting or hot extrusion.^[11,13–15]

However, a detailed understanding of the microstructure-dependent corrosion mechanism, which will enable the optimization of the medium- and long-term degradation behavior,

1. Introduction


Mg–Ca–Zn alloys have become increasingly important as potential biodegradable materials for orthopaedic applications.

Prof. D. Zander, Dr. N. A. Zumdick, M. Felten, Dr. C. Schnatterer, Dr. V. F. Chaineux
Division of Materials Science and Engineering
RWTH Aachen University
Intzestraße 5, 52072 Aachen, Germany
E-mail: d.zander@gi.rwth-aachen.de

Dr. P. Zaslansky
Department for Operative and Preventive Dentistry
Charité – Universitätsmedizin Berlin
Aßmannshauser Str. 4-6, 14197 Berlin, Germany

Dr. J. U. Hammel, Dr. M. Storm, Dr. F. Wilde
Helmholtz-Zentrum Hereon Institute for Materials Physics
Max-Planck-Str. 1, 21502 Geesthacht, Germany

Prof. C. Fleck
Institute of Material Sciences and Technology, Chair of Materials Science & Engineering
Technische Universität Berlin
Straße des 17. Juni 135, 10623 Berlin, Germany

 The ORCID identification number(s) for the author(s) of this article can be found under <https://doi.org/10.1002/adem.202100157>.

© 2021 The Authors. Advanced Engineering Materials published by Wiley-VCH GmbH. This is an open access article under the terms of the Creative Commons Attribution-NonCommercial-NoDerivs License, which permits use and distribution in any medium, provided the original work is properly cited, the use is non-commercial and no modifications or adaptations are made.

DOI: 10.1002/adem.202100157

remains unresolved. Therefore, an investigation of the influence of the 3D microstructural architecture on the corrosion of biodegradable Mg–Ca–Zn alloys is necessary.

Importantly, the specific corrosion mechanism of low-alloyed Mg–Ca–Zn alloys strongly depends on the local chemical composition and the 3D microstructural architecture, comprising the type, volume fraction, distribution, 3D morphology, and connectivity of different phases and the interfaces between them. It has been reported that primary magnesium phase (α -Mg_{ss}) and secondary phases, namely, Mg₂Ca and Mg₆Ca₂Zn₃, are formed in low-alloyed Mg–Ca–Zn alloys during solidification.^[14,15] However, the final composition of the ternary Mg–Ca–Zn phase is still under an ongoing controversial discussion.^[16] Furthermore, it has been reported that the different phases serve as both corrosion barriers and corrosion accelerators due to the formation of heterogeneous mixed electrodes at the surfaces, resulting in microgalvanic coupling.^[11,17–20] The mixed electrodes are formed due to different activities of the secondary phases, with the electrochemical activity increasing in the order of Mg₂Ca > α -Mg > Ca₃Mg_xZn_{15–x}, $4.6 \leq x \leq 12$.^[17] The dualism of intermetallic phases has, to date, mainly been investigated with 2D methods, which have provided valuable insights into certain aspects of the mechanisms acting between different phases at the surface. However, they merely provide limited information on the role of the 3D microstructural features and on the locally distributed and accelerated heterogeneous corrosion attack. This information is sorely required for a comprehensive understanding and control of the in vitro corrosion mechanism from strongly localized toward more uniformly distributed heterogeneous electrode processes of biodegradable Mg–Ca–Zn alloys.

The 3D microstructures of several Mg alloys have been investigated by synchrotron radiation-based microtomography (SR- μ CT) before and after in vitro or in vivo corrosion.^[21–23] Although a few reports on SR- μ CT have addressed the in vivo corrosion state of biodegradable Mg–Ca–Zn alloys,^[24–27] a detailed 3D study of the in vitro corrosion behavior of magnesium alloys has not been conducted. The present study focuses on bridging the gap between ex situ 2D methods and quasi in situ immersion 3D SR- μ CT for the characterization of biodegradable low-alloyed Mg–Ca–Zn alloys. In particular, the utilization of 3D SR- μ CT after quasi in situ immersion in Hanks' balanced salt solution (HBSS) without glucose provides a deeper insight into the complex relationship between the 3D microstructural architecture and the dynamic corrosion mechanisms of low-alloyed Mg–Ca–Zn.

2. Experimental Section

2.1. Material Selection and Preparation

Three alloys with the nominal composition Mg–0.6 wt% Ca–0.8 wt% Zn (ZX11), Mg–0.6 wt% Ca–1.8 wt% Zn (ZX21), and Mg–1.2 wt% Ca–3.6 wt% Zn (ZX41) were produced using the gravity die casting process reported in Zander and Zumdick.^[11] Table 1 shows an overview of the impurity content, analyzed by spark optical emission spectroscopy (OES).

From the Mg–Ca–Zn castings, specimens were manufactured by turning, grinding up to a grit size of 4000, and a subsequent final cleaning in an ultrasonic bath with acetone. The specimens had a final dimension of 1.5 mm diameter and 2 mm height.

2.2. Quasi In Situ Corrosion

The Mg–Ca–Zn alloys were analyzed with SR- μ CT before and after quasi in situ immersion in 200 mL HBSS at 37 °C. The electrolyte was prepared using high-purity chemicals and double-distilled water as recommended in previous studies^[28,29] (Table 2).

The quasi in situ immersion experiments of the Mg–Ca–Zn alloys were initially performed for 8 h. After a subsequent removal from the electrolyte, the specimens were rinsed with bidistilled water and examined by SR- μ CT. This entire procedure was repeated for the same specimen with an additional immersion time of 16 h with freshly prepared electrolyte, to achieve a total immersion time of 24 h and defined as a quasi in situ experiment.

Table 2. Chemical compounds of HBSS without glucose.^[28,29]

HBSS without glucose			
Anorganic compound	[mg L ^{−1}]	Chemical compound	[mmol L ^{−1}]
NaCl	8000	Na ⁺	142.0
KCl	400	K ⁺	5.9
Na ₂ HPO ₄	48	Ca ²⁺	1.3
KH ₂ PO ₄	60	Mg ²⁺	0.8
MgSO ₄ ·7H ₂ O	200	HCO ₃ [−]	4.2
NaHCO ₃	350	Cl [−]	145.0
CaCl ₂	140	HPO ₄ ^{2−}	0.8
		SO ₄ ^{2−}	0.8

Table 1. Impurity content of as-cast low-alloyed Mg–Ca–Zn analyzed by spark OES.

	Al [wt%]	Mn [wt%]	Si [wt%]	Fe [wt%]	Cu [wt%]	Ni [wt%]	Fe/Mn [wt%]
Mg–0.6 wt% Ca–0.8 wt% Zn (ZX11) Zn/Ca = 0.82	0.0120	0.0183	0.0222	0.0006	0.0005	0.0021	0.0328
Mg–0.6 wt% Ca–1.8 wt% Zn (ZX21) Zn/Ca = 1.84	0.014	0.0069	0.0229	0.0006	0.0006	0.0021	0.0874
Mg–1.2 wt% Ca–3.6 wt% Zn (ZX41) Zn/Ca = 1.84	0.026	0.0066	0.0291	0.0006	0.0006	0.0021	0.0913

2.3. Material Characterization

A Zeiss Supra 55 VP Ultim Max scanning electron microscope including an energy-dispersive X-ray spectroscope (Oxford Instruments) was used for 2D microstructural analysis of the cast Mg–Ca–Zn alloys before and after corrosion.

High-density-resolution microtomography was conducted at the imaging beamline (IBL) P05^[30–32] operated by the Helmholtz–Zentrum Geesthacht at the storage ring PETRA III located at “Deutsches Elektronen-Synchrotron” (DESY) in Hamburg, Germany. A photon energy of 16 keV was applied for imaging under absorption contrast conditions, with additional imaging using propagation-based edge enhancement using sample-detector distances of 7, 8, and 30 mm. For each measurement, 1527 projection images were acquired with a final pixel size of 1.2 μm . The exposure time per projection was set to either 750 or 950 ms. Data preprocessing and reconstruction were performed using the P05 IDL-based reconstruction pipeline with a filtered back-projection reconstruction algorithm. Low-contrast datasets were further processed and reconstructed using the Charite Octave-based reconstruction pipeline, where filtered back projection was

computed using nRecon (v 1.6, Bruker-microCT, Kontich, Belgium).

To examine the as cast 3D microstructure, the acquired images were visualized using the VG StudioMax software from Volume Graphics. A software-integrated Gaussian filter was applied and a manual segmentation of the different secondary phases was performed via an implemented threshold-based surface detection. With the determined threshold, the corresponding phase fraction in the volume was evaluated via the gray value histogram of the reconstructed 3D microstructure. **Figure 1** schematically shows the applied workflow of the microstructural analysis of the tomographic data on the example of ZX11. The 2D EDS mappings for Mg, Ca, and Zn were used to provide evidence of the occurrence of two different secondary phases in the microstructure. The zinc content in the intermetallic phases served as an initial indicator for differentiating the intermetallic phases. By visualization of the synchrotron data, 3D images of the specimens were nondestructively acquired, enabling the analysis of the internal microstructure in the volume through cross-sections. Thereafter, the segmentation process was used to separately display the secondary phases without the matrix. Thus, 3D subvolumes were extracted and analyzed.

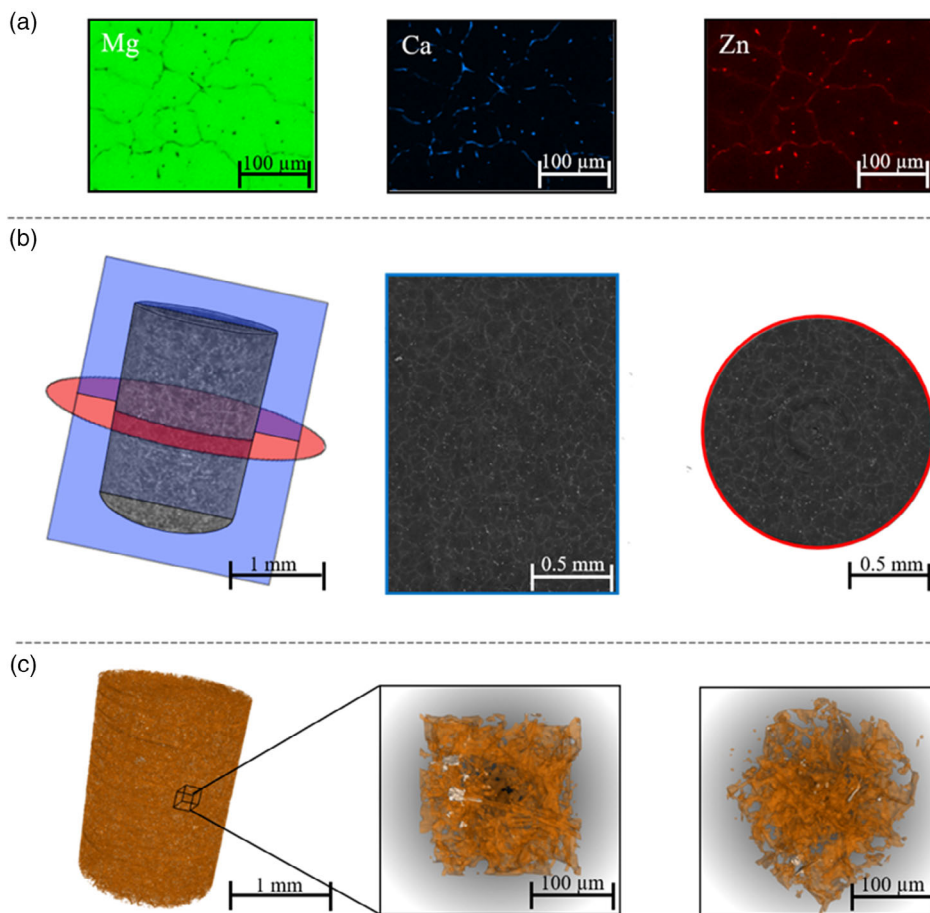


Figure 1. Workflow to visualize the microstructure of low-alloyed Mg–Ca–Zn by SR-μCT, exemplarily shown for ZX11. a) EDS mappings, b) 3D visualization including slices, and c) secondary phase volume fraction rotated around the z- and x-axes.

3. Results

3.1. Microstructural Characterization of Mg–Ca–Zn Alloys before Corrosion

The 2D scanning electron microscopy (SEM) studies (Figure 2) show two distinct secondary phases occurring in the microstructure of all analyzed alloys. These phases were assigned to the $\text{Mg}_6\text{Ca}_2\text{Zn}_3$ or $\text{Ca}_3\text{Mg}_x\text{Zn}_{15-x}$, $4.6 \leq x \leq 12$, phase and the Mg_2Ca phase including dissolved Zn in previous studies by means of energy dispersive X-ray spectroscopy (EDS) and X-ray diffraction (XRD).^[11,16,33–35] However, ZX11 exhibits predominantly the Mg_2Ca phase with dissolved Zn as a secondary phase, which is either arranged along the grain boundaries of the magnesium dendrites or as a granular-shaped secondary phase within the primary magnesium phase. Further, the ternary $\text{Ca}_3\text{Mg}_x\text{Zn}_{15-x}$, $4.6 \leq x \leq 12$, phase is present in the ZX11 alloy. The SEM studies indicate the coexistence and interlinked occurrence of both secondary phases. This is in good agreement with observations reported in the literature for low-alloyed Mg–Ca–Zn with a Zn/Ca ratio of less than 1.2.^[36] In contrast to ZX11, an additional eutectic microstructure is visible for the alloys ZX21 and ZX41. Furthermore, the change toward a eutectic microstructure goes along with the formation of an increased number of eutectic junctions, indicating a change of a 2D semicontinuous network to a continuous network from ZX21 to ZX41. Previous studies already showed that the eutectic microstructure consists of $\alpha\text{-Mg}_{\text{SS}}$ and $\text{Mg}_6\text{Ca}_2\text{Zn}_3$.^[37] In this work, the SEM investigations (Figure 2) reveal that the $\alpha\text{-Mg}_{\text{SS}}$ is continuously encapsulated by the ternary phase.

The 2D SEM results on the secondary phase formation assisted the 3D data visualization of the reconstructed data obtained by SR- μCT . The threshold-based detection of the 3D volumes also revealed two distinct secondary phases in all investigated alloys. These phases were subsequently assigned to the binary $(\text{Mg,Zn})_2\text{Ca}$ phase and the ternary $\text{Ca}_3\text{Mg}_x\text{Zn}_{15-x}$, $4.6 \leq x \leq 12$, phase according to the EDS evaluations and literature data.^[11,33–35] Table 3 provides the quantitative results of the secondary-phase volume fractions as a function of alloy composition. The largest volume fraction in ZX11 is assigned to the $(\text{Mg,Zn})_2\text{Ca}$ phase, and the largest volume fraction in ZX21 and ZX41 is assigned to the $\text{Ca}_3\text{Mg}_x\text{Zn}_{15-x}$, $4.6 \leq x \leq 12$, phase. Although alloy ZX21 contains a higher content of alloying elements as compared to ZX11, it exhibits the

Table 3. Nominal ratio of zinc and calcium in the alloys, as well as the volume phase fractions of the secondary phases determined by gray values from the reconstructed volumes.

Alloy	Atomic Zn/Ca ratio [–]	$([\text{Mg}], \text{Ca}_3\text{Mg}_x\text{Zn}_{15-x}, (\text{Mg,Zn})_2\text{Ca})$ [%vol]	$4.6 \leq x \leq 12$ [%vol]	Σ Phase fraction sec. phase [%vol]
Mg–0.6 wt% Ca–0.8 wt% Zn (ZX11)	0.82	13.9	0.4	14.3
Mg–0.6 wt% Ca–1.8 wt% Zn (ZX21)	1.84	1.1	6.8	7.9
Mg–1.2 wt% Ca–3.6 wt% Zn (ZX41)	1.84	3.5	10.9	14.4

lowest total content of secondary phases. Moreover, comparing the total phase fractions of ZX41 and ZX21, which exhibit the same ratio of Zn/Ca, but a two times higher nominal content of the alloying elements, an approximate doubling of the total phase fraction was observed. However, the proportion of the $(\text{Mg,Zn})_2\text{Ca}$ phase increased disproportionately by a factor of three.

Figure 3 shows the 3D network of the intermetallic phases contained in the microstructure of the entire reconstructed volumes after the segmentation procedure and elimination of the matrix. The 3D visualization indicates that the secondary phases form a continuous interconnected network for all alloys investigated.

The formation of a continuous network was confirmed by slices through the reconstructed 3D volumes of ZX11, ZX21, and ZX41 (Figure 4).

The 3D network of alloy ZX11 is predominantly formed by the $(\text{Mg,Zn})_2\text{Ca}$ phase (Figure 3, orange) and partially interrupted by the coexisting $\text{Ca}_3\text{Mg}_x\text{Zn}_{15-x}$, $4.6 \leq x \leq 12$, phase (Figure 3, white). In contrast, the continuous 3D network of ZX21 is dominated by the ternary $\text{Ca}_3\text{Mg}_x\text{Zn}_{15-x}$, $4.6 \leq x \leq 12$, phase. However, coexisting small and thin rod-shaped sections in the network are additionally formed by the $(\text{Mg,Zn})_2\text{Ca}$ phase, whereas the 3D network of the intermetallic phases in ZX41 is characterized by significantly thicker, contiguous sections of the $(\text{Mg,Zn})_2\text{Ca}$ phase compared with alloy ZX21. These $(\text{Mg,Zn})_2\text{Ca}$ sections are not separated from each other, but rather form a coherent area structure. Therefore, this characteristic structure

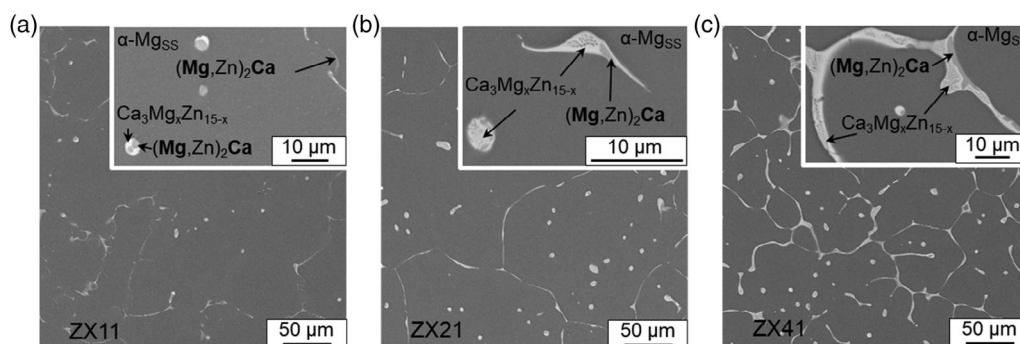


Figure 2. SEM images of the microstructure of a) ZX11, b) ZX21, and c) ZX41.

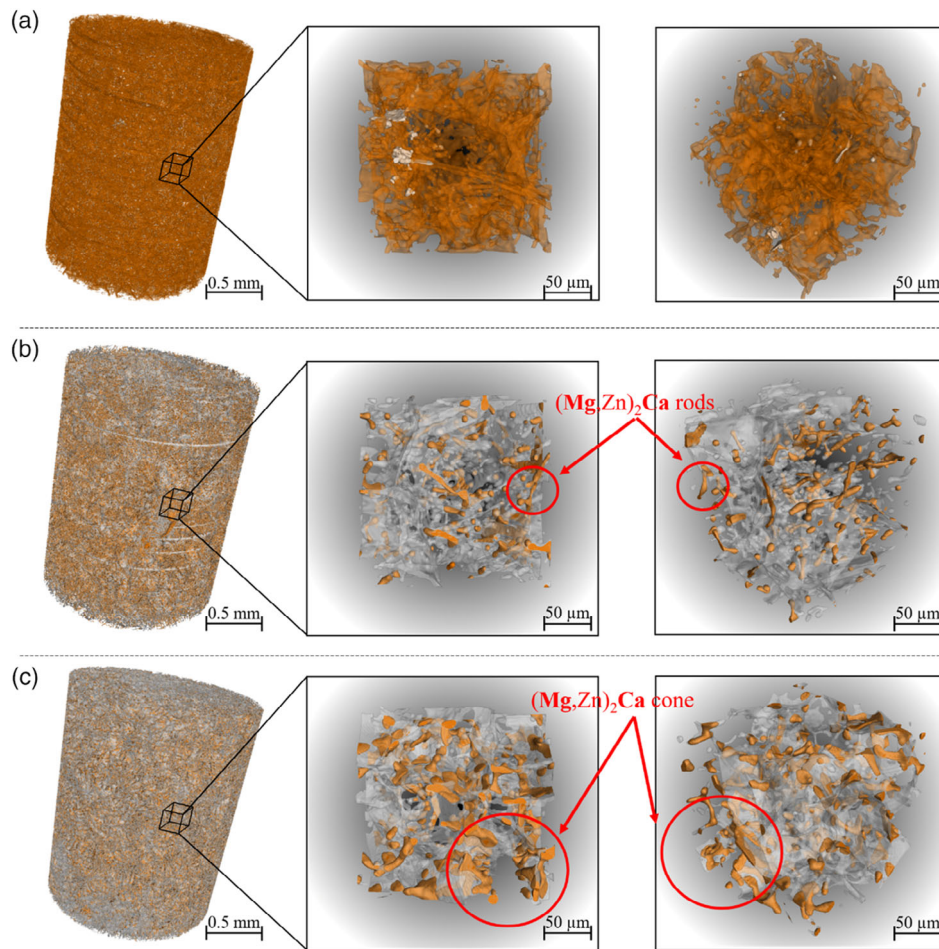


Figure 3. 3D visualization of the secondary phases ($(\text{Mg,Zn})_2\text{Ca}$ = orange, $\text{Ca}_3\text{Mg}_7\text{Zn}_{15-x}$, $4.6 \leq x \leq 12$ = white) in the entire investigated volume (left), as well as the corresponding subvolumes in the surface view (middle) and the vertex view (right) of the alloys a) ZX11, b) ZX21, and c) ZX41.

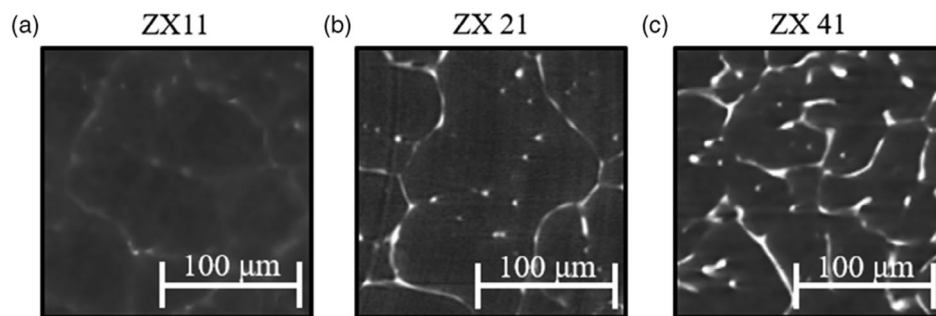


Figure 4. Slices of the reconstructed 3D volume obtained via SR- μ CT of the secondary phases: $(\text{Mg,Zn})_2\text{Ca}$ and $\text{Ca}_3\text{Mg}_7\text{Zn}_{15-x}$, $4.6 \leq x \leq 12$, of the alloys a) ZX11, b) ZX21, and c) ZX41.

leads to an increased interface between the matrix and the $(\text{Mg,Zn})_2\text{Ca}$ phase. In the lower right corner of the surface view from the subvolume in Figure 3c, this $(\text{Mg,Zn})_2\text{Ca}$ area-like structure even forms a kind of cone (see red circle), which extends into the matrix and provides a potential widespread material susceptibility to a corrosion attack due to the ignoble nature of the $(\text{Mg,Zn})_2\text{Ca}$ phase.

3.2. Microstructural Characterization of Mg–Ca–Zn Alloys after Quasi In Situ Immersion

Figure 5 shows the visualized volumes of the SR- μ CT investigations of ZX11, ZX21, and ZX41 before and after the quasi in situ immersion experiments for 8 h and a total of 24 h in the HBSS electrolyte. ZX11 exhibits the most pronounced corrosive

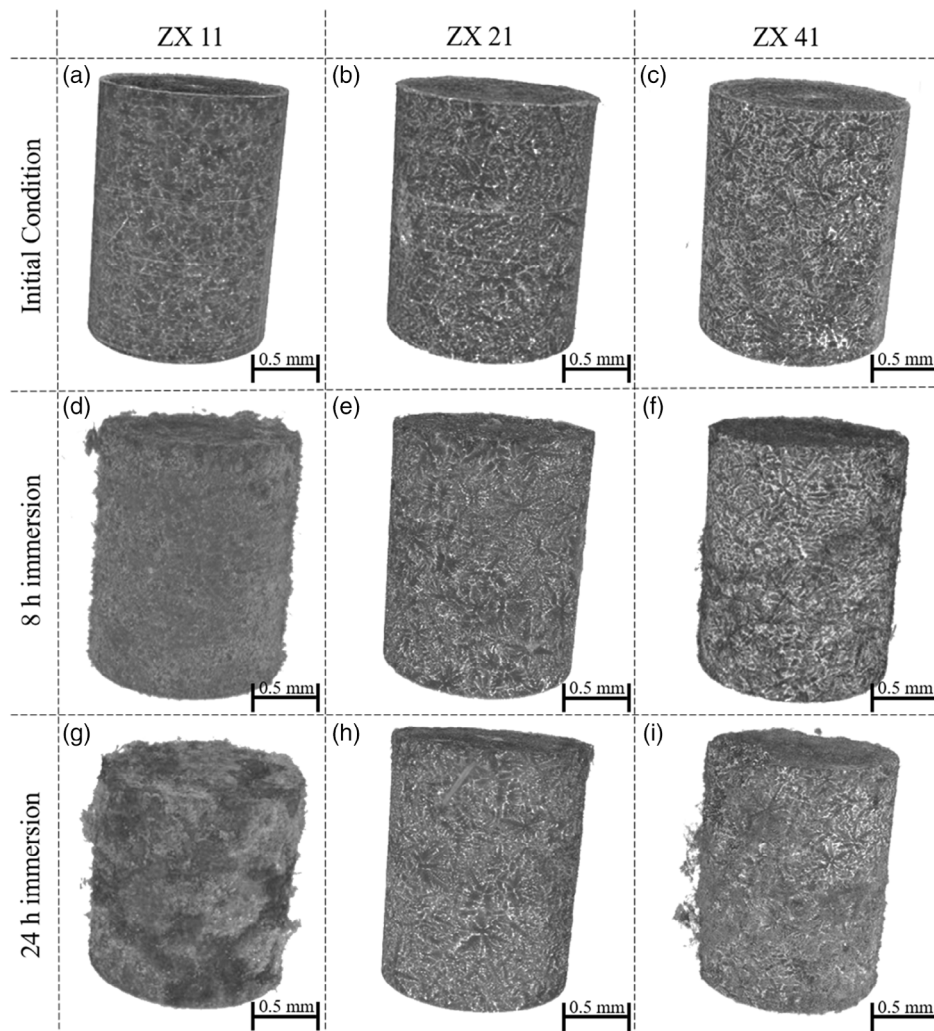


Figure 5. Visualization of the reconstructed 3D images of ZX11, ZX21, and ZX41 in the a–c) initial condition, d–f) after 8 h immersion, and g–i) after a total of 24 h quasi in situ immersion in HBSS.

damage after an immersion time of 8 h among investigated alloys. The corrosion products form a relatively thick and voluminous layer over the entire surface of the specimen. In contrast, after the same immersion time, ZX21 shows almost no macroscopically visible corrosion phenomena with associated corrosive products. ZX41 exhibits a locally strong, limited selective corrosive attack with the associated accumulation of corrosion products after the same immersion time. Moreover, the observed trend becomes even more pronounced after a total immersion time of 24 h for all investigated alloys. The corrosion products of ZX11 form a continuous and even more voluminous layer on the whole surface of the specimen after 24 h; thus, the microstructure of the secondary phases is not visible from outside.

Slices (**Figure 6**) of the previously presented volumes exhibit even more detailed formation of heterogeneous electrode processes and the formation of corrosion product layers. It is evident that the corrosion attack is significantly localized for ZX11 compared to ZX21 and ZX41 after a quasi in situ

immersion time of 8 h and a total of 24 h. Furthermore, a mechanistic change in the microstructure-dependent corrosion process is assumed for ZX21 compared to ZX41 because ZX21 shows rather uniform and less pronounced heterogeneous corrosion reactions.

Additional 2D SEM investigations of ZX11, ZX21, and ZX41 for 2 h immersion in HBSS (**Figure 7**) were conducted to gain a deeper insight into the corrosion initiation mechanism. Similar to the 3D SR- μ CT investigations, the 2D SEM cross-sections revealed that ZX11 forms the most voluminous corrosion product layer at the surface in comparison to ZX21 and ZX41. This voluminous corrosion product layer is also related to a more pronounced localized corrosion. However, even the Mg–Ca–Zn alloy with the highest Ca and Zn contents occasionally shows the formation of a voluminous corrosion product layer as a consequence of pronounced heterogeneous anodic electrode processes on the surface, in addition to a rather homogeneously distributed local corrosion attack. Surprisingly, ZX21 revealed merely a partially detectable corrosion product layer by the 3D synchrotron

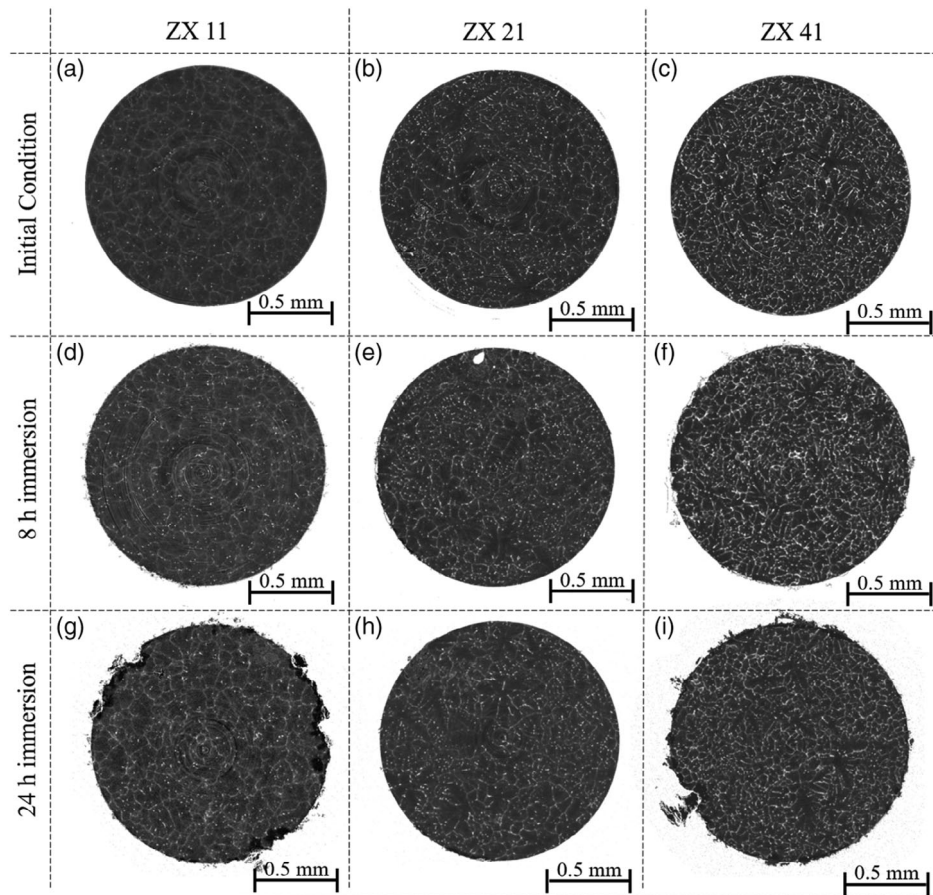


Figure 6. Slices through the 3D volumes of Figure 5 for ZX11, ZX21, and ZX41 in the a–c) initial condition, d–f) after 8 h immersion, and g–i) after a total of 24 h immersion in HBSS.

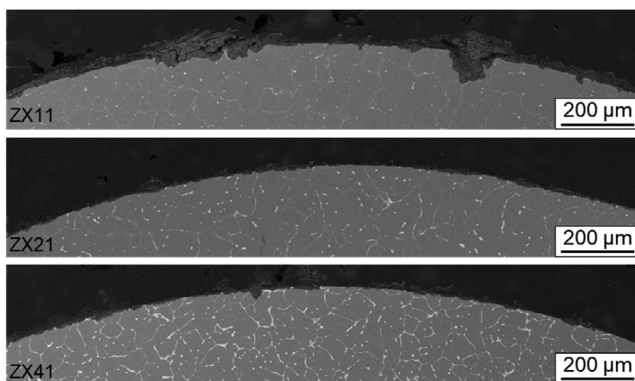


Figure 7. Scanning electron micrographs of the microstructure of ZX11, ZX21, and ZX41 after immersion for 2 h in HBSS.

phase contrast tomography investigations shown in Figure 6, as well as in the SEM examinations shown in Figure 7, after an immersion time of 2 h. An almost uniformly distributed heterogeneous electrode process was observed, which led to a homogeneous diameter loss as well as to the homogeneous formation of a corrosion product layer on the surface.

A characteristic SEM-EDS cross-section of the microstructure, including all three phases, namely α -Mg_{SS}, (Mg,Zn)₂Ca, and the coexisting $\text{Ca}_3\text{Mg}_x\text{Zn}_{15-x}$, $4.6 \leq x \leq 12$, phase of ZX21 after immersion up to 2 h in HBSS is shown in Figure 8. It is evident that anodic corrosion processes lead to local dissolution of the α -Mg_{SS} and (Mg,Zn)₂Ca coexisting with the $\text{Ca}_3\text{Mg}_x\text{Zn}_{15-x}$, $4.6 \leq x \leq 12$, phase and subsequently to the formation of a magnesium–calcium-based oxide or hydroxide. In addition, an accumulation of magnesium, calcium, carbon, and phosphorus was observed above the oxide close to the Mg–Ca–Zn alloy/electrolyte interface. Anodic dissolution of zinc-rich regions near the surface, in particular the ternary $\text{Ca}_3\text{Mg}_x\text{Zn}_{15-x}$, $4.6 \leq x \leq 12$, phase, could not be observed by SEM-EDS, due to its limited resolution.

4. Discussion

4.1. Influence of Alloying Elements on 3D Microstructural Architecture of As-Cast Mg–Ca–Zn Alloys

The specific corrosion mechanisms of low-alloyed Mg–Ca–Zn alloys strongly depend on the local chemical composition and the 3D microstructural architecture, comprising the type,

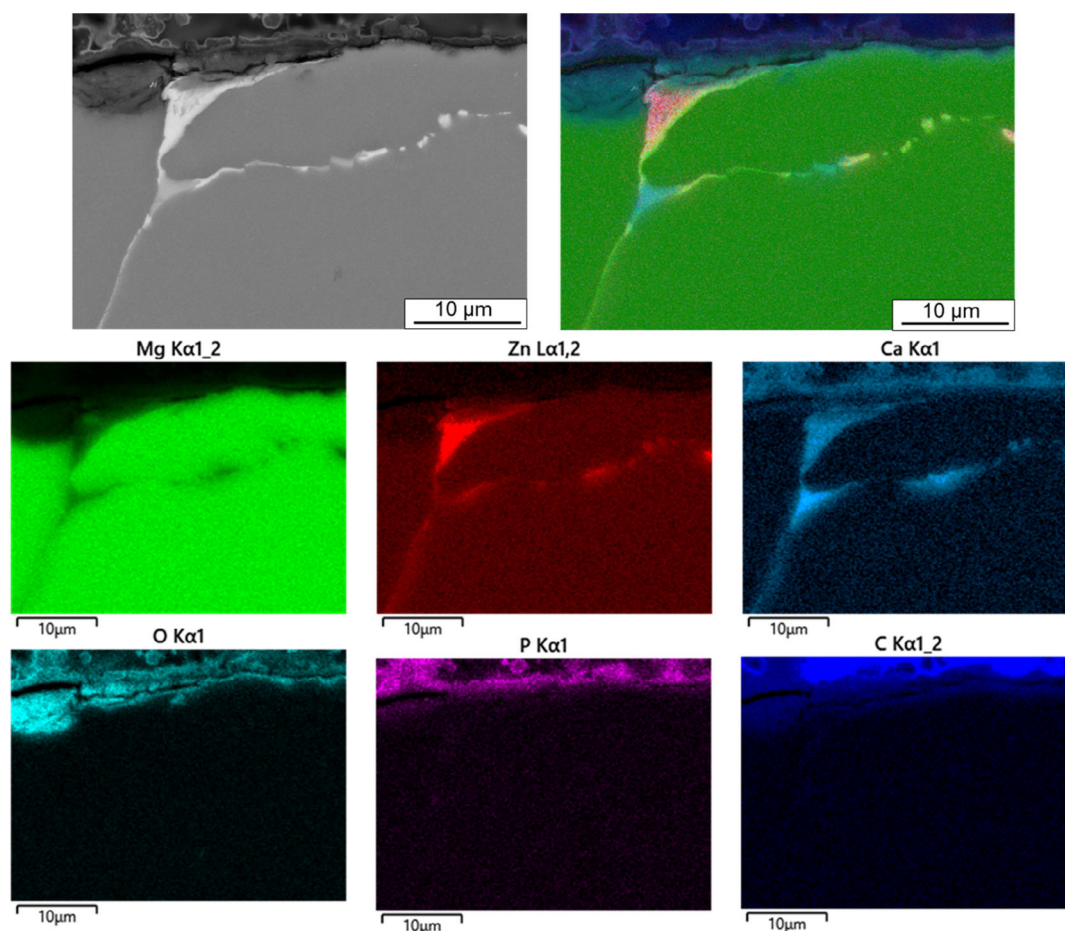


Figure 8. SEM-EDS images of ZX21 after corrosion for 2 h in HBSS.

fraction, morphology, distribution, connectivity, and interfaces of different phases. Therefore, analysis of these microstructural features is of significant importance and was therefore of major focus in this study. Previous studies of low-alloyed Mg–Ca–Zn^[11] revealed an enrichment of Zn and Ca in α -Mg_{SS} with increasing alloying element content. Furthermore, it was reported that when the Zn/Ca ratio is less than 1.2 or 1.4, a microstructure with three phases, comprising the primary α -Mg_{SS} phase, the secondary (Mg,Zn)₂Ca phase, and the Mg–Ca–Zn phase, is formed, whereas at Zn/Ca ratios above 1.2, only two phases are formed, namely, the α -Mg_{SS} phase and the secondary Mg–Ca–Zn phase.^[36,38,39] However, the exact composition of the ternary Mg–Ca–Zn phase remains controversial. Formation of $\text{Ca}_3\text{Mg}_x\text{Zn}_{15-x}$, $4.6 \leq x \leq 12$,^[16] of $\text{Ca}_2\text{Mg}_6\text{Zn}_3$,^[37,39-41] $\text{Ca}_2\text{Mg}_5\text{Zn}_5$,^[42,43] $\text{Ca}_2\text{Mg}_5\text{Zn}_{13}$,^[40] or IM1-4^[44] has been proposed.

The current study confirmed the formation of α -Mg_{SS}, (Mg,Zn)₂Ca, and $\text{Ca}_3\text{Mg}_x\text{Zn}_{15-x}$, $4.6 \leq x \leq 12$, in as-cast ZX11 with a Zn/Ca ratio of 0.82, by 2D and 3D methods. However, a Zn/Ca ratio of 1.84 for as-cast ZX21^[11] and for as-cast ZX41 also revealed formation of α -Mg_{SS}, (Mg,Zn)₂Ca and $\text{Ca}_3\text{Mg}_x\text{Zn}_{15-x}$, $4.6 \leq x \leq 12$, which contradicts calculations of the ternary Mg–Ca–Zn phase diagram^[38] as well as previous observations reported by Zhang and Yang^[36] on cast Mg–Zn–Mn–Ca alloys.

However, the investigations of Li et al.^[37] on as-cast low-alloyed Mg–Ca–Zn with a Zn/Ca ratio of 1.9 are in good agreement with this current study and confirm the formation of two secondary phases in addition to primary magnesium. In contrast, a microstructure consisting exclusively of a single secondary $\text{Ca}_2\text{Mg}_6\text{Zn}_3$ phase has been reported at a significantly higher Zn/Ca ratio of 6.3.^[37] These controversial observations indicate a non-negligible influence of the casting process parameters, such as melting temperature and cooling rate, on the precipitation sequence, which must be taken into account in further investigations on the solidification of Mg–Ca–Zn alloys.

Considering in addition the influence of the total alloying element concentrations on the secondary-phase formation, this study shows that an increasing Zn content leads to a higher volume fraction of the $\text{Ca}_3\text{Mg}_x\text{Zn}_{15-x}$, $4.6 \leq x \leq 12$ phase and a lower volume fraction of the (Mg,Zn)₂Ca phase. This is assumed to be correlated with the mixing enthalpy between Zn and Ca, which was reported to be -22 kJ mol^{-1} larger compared to Zn and Mg or Ca and Mg.^[45] Therefore, the formation of the ternary phase in comparison with the (Mg,Zn)₂Ca phase becomes more likely with increasing Zn content.^[37]

The current investigations revealed that the solidification of low-alloyed Mg–Ca–Zn is accompanied by an increased

formation of an additional eutectic microstructure with increasing Zn content. Previously published transmission electron microscopy (TEM) investigations by Li et al.^[37] confirmed that the observed eutectic microstructure is composed of α -Mg_{SS} and Ca₂Mg₆Zn₃ and that this is related to the greater diffusivity of Ca in Mg.^[46,47] Therefore, it is assumed that the observed seam of Ca₃Mg_xZn_{15-x}, $4.6 \leq x \leq 12$, surrounding the eutectic α -Mg_{SS} in as-cast ZX21 and ZX41 is also strongly related to the preferred diffusion processes of Ca in α -Mg_{SS}. This may lead to the formation of an increased number of eutectic junctions and in an increase in the width and fraction of the secondary phases for ZX41. However, not much was known until now about the 3D morphology and the total and single volume fraction of the secondary phases as well as the continuity of the network formed by the secondary phases of as-cast low-alloyed Mg–Ca–Zn.

In this work, the utilization of SR- μ CT analysis has made it possible to perform a quantitative analysis of the volume phase fraction of the individual secondary phases as well as for the total secondary phases of low-alloyed Mg–Ca–Zn. A significant change of the volume phase fraction of the (Mg, Zn)₂Ca phase from about 14%_{Vol} to 1%_{Vol} was observed for ZX11 and ZX21 by increasing the Zn content by only 1 wt%, while changing the Zn/Ca atomic ratio from 0.82 to 1.84. This is attributed to the mentioned larger mixing enthalpy between Zn and Ca compared to Zn and Mg or Ca and Mg. Surprisingly, a constant Zn/Ca atomic ratio of 1.84 and a two times higher Ca and Zn content in ZX41 compared to ZX21 revealed a disproportional factor for the (Mg, Zn)₂Ca volume phase fraction. In addition, a significant growth and formation of a coherent area structure of the (Mg, Zn)₂Ca phase, which resulted in an increased interface between the primary α -Mg_{SS} and the (Mg, Zn)₂Ca phase, was observed for ZX41. This accelerated growth, driven by the preferred diffusion of Ca in Mg, is assumed to change the proportionality that would potentially be expected if Zn and Ca contents were doubled. However, the higher number of (Mg, Zn)₂Ca nucleation sites is assumed to result in a higher amount of about 11%_{Vol} Ca₃Mg_xZn_{15-x}, $4.6 \leq x \leq 12$, phase in ZX41 in comparison to about 7%_{Vol} observed in ZX21.

2D imaging methods were previously used to show that the total fraction of the secondary phases increases with increasing zinc and calcium content.^[11] The nondestructive 3D evaluation of the investigated Mg–Ca–Zn alloys revealed a significantly different picture compared to the assumptions obtained by 2D analysis regarding the dependence of the total phase fraction on the Ca and Zn content. The results show only a proportional increase from about 8%_{Vol} to 14%_{Vol} of the total volume phase fraction of the secondary phases with the proportional increase of the Ca and Zn content at a constant Zn/Ca atomic ratio. At much lower Ca and Zn contents investigated for ZX11, a high total volume phase fraction of the secondary phases of about 14.3%_{Vol}, similar to ZX41, was observed.

A continuous 3D network of secondary phases was observed in all the studied alloys. This is in contradiction to the 2D observations of a semicontinuous network, which becomes continuous with increasing Zn content and underlines the high significance of the performed SR- μ CT investigations.

4.2. Influence of 3D Microstructural Architecture and Local Chemical Composition on the Corrosion Mechanism of As-Cast Mg–Ca–Zn Alloys

The SR- μ CT images showed that different 3D microstructural architectures, consisting of different total volume fractions of the secondary phases and volume fractions of the single secondary (Mg, Zn)₂Ca and Ca₃Mg_xZn_{15-x}, $4.6 \leq x \leq 12$, phases, morphologies, network continuity, and interfacial properties of secondary phases, lead to different corrosion mechanisms. It is known that the corrosion initiation and growth depend strongly on the electrochemical activity of the present phases in low-alloyed Mg–Ca–Zn. It was reported that the electrochemical activity increases in the order Mg₂Ca > α -Mg > Ca₃Mg_xZn_{15-x}, $4.6 \leq x \leq 12$.^[17] Therefore, the corrosion mechanisms of Mg–Ca–Zn alloys were associated with the formation of microgalvanic elements in conjunction with heterogeneous electrode processes where, e.g., (Mg, Zn)₂Ca starts to dissolve and is therefore assumed to initiate the corrosion process. Further, it was reported that the formation of a (Mg, Zn)₂Ca phase at high Zn content will decrease the corrosion rate by increasing the electrochemical potential close to α -Mg_{SS}.^[19] The Ca₃Mg_xZn_{15-x}, $4.6 \leq x \leq 12$, phase in contrast is assumed to act either as a corrosion accelerator or barrier during the dissolution of (Mg, Zn)₂Ca and α -Mg_{SS}, depending on the continuity of the secondary phase network obtained by the ternary phase.^[11,20] However, in addition to the electrochemical activity of the present phases, the 3D microstructural architecture as well as the dynamically changing corrosion reactions with time have to be considered to describe the specific corrosion mechanism.

The SR- μ CT investigations of ZX11 revealed the strongest localized corrosion attack as well as the formation of a thick and voluminous corrosion product layer after 24 h immersion time in HBSS compared to ZX21 and ZX41. The 3D investigations of ZX11 revealed a volume phase fraction of about 14%_{Vol} of a continuous (Mg, Zn)₂Ca network, which is assumed to act as a corrosion initiation site, followed by the dissolution of the adjacent magnesium matrix. It was reported^[20] for nanocrystalline Mg–0.3 wt% Ca–1.0 wt% Zn (ZX10) that the Mg₂Ca phase or (Mg, Zn)₂Ca itself is assumed to act as the initiation site by a dealloying mechanism.^[20] Therefore, Ca will dissolve first followed by Mg from the (Mg, Zn)₂Ca phase. In general, these assumptions should lead to a homogeneously distributed localized corrosion attack within short immersion times. This is in contradiction to the accelerated locally distributed heterogeneous corrosion reactions with the formation of deeper corrosion damage of ZX11 compared to ZX21 and ZX41. This is assumed to be related to the additionally formed Ca₃Mg_xZn_{15-x}, $4.6 \leq x \leq 12$. Despite its low volume phase fraction of 0.4%_{Vol}, the phase acts as additional cathodic element. Thus it adds to creating a microgalvanic element, increasing locally the driving force for the dissolution, of the coexisting (Mg, Zn)₂Ca phase and/or the adjacent α -Mg_{SS}.

The present study reveals that the alloys ZX21 and ZX41 exhibit a significant change in the 3D microstructural architecture compared to ZX11. The SR- μ CT investigations show no significant formation of a corrosion product layer and a more

uniform heterogeneous corrosion process for ZX21 compared to ZX41. The cross-sectional changes, evident in the slices of the visualized volume after quasi in situ immersion up to 8 h and a total of 24 h, as well as the SEM studies after 2 h of immersion, are smaller for ZX21 than for ZX41. Furthermore, the 3D visualization of the secondary phases shows the coexistence of $(\text{Mg}, \text{Zn})_2\text{Ca}$ and $\text{Ca}_3\text{Mg}_x\text{Zn}_{15-x}$, $4.6 \leq x \leq 12$, within a continuous network for both alloys. In addition, a smaller size of the secondary phases as well as a higher volume fraction of 3.5%_{vol} of the rod-shaped $(\text{Mg}, \text{Zn})_2\text{Ca}$ phase in ZX21 compared to the coherent plate like $(\text{Mg}, \text{Zn})_2\text{Ca}$ phase with a volume fraction of 1.1%_{vol} in ZX41 was observed. Therefore, it may be concluded that the heterogeneous corrosion process is also dependent on the size, distribution, and morphology of the $(\text{Mg}, \text{Zn})_2\text{Ca}$ phase influencing the fraction of interfaces between the binary phase and the $\alpha\text{-Mg}_{\text{SS}}$.

The accelerated uniformly distributed heterogeneous corrosion reactions for ZX41 compared to ZX21 are dependent on the higher volume phase fraction of the continuous $\text{Ca}_3\text{Mg}_x\text{Zn}_{15-x}$, $4.6 \leq x \leq 12$, network, partially coexisting with the $(\text{Mg}, \text{Zn})_2\text{Ca}$ phase. Recently, TEM studies on the dissolution ability of the isolated nanocrystalline IM1 phase in Mg–0.25 wt% Ca–1.5 wt% Zn were published.^[20,48] This dissolution behavior was related to a cathodically polarized dealloying mechanism, which causes a preferential dissolution of Ca and Mg. The retained Zn was assumed to be embedded in the corrosion layer. After further dissolution of the retained Zn, a redeposition on the corroding surface was proposed. This may lead to local acceleration of corrosion reactions in addition to the secondary-phase-driven corrosion mechanisms. The SEM-EDS measurements of the exemplarily shown ZX21 after 2 h immersion time did not confirm this observation. Further investigations are currently in progress. In addition, ZX41 exhibits coherent area structures leading to a distinctly increased interface between the magnesium matrix and the $(\text{Mg}, \text{Zn})_2\text{Ca}$ phase. Specifically, the additional formation of cone-like interfaces between $(\text{Mg}, \text{Zn})_2\text{Ca}$ and $\alpha\text{-Mg}_{\text{SS}}$ provides an additional material susceptibility to a localized corrosion attack, which was also observed for ZX41 in contrast to ZX21.

However, recent results^[11,35] showed that ZX11 exhibits the lowest mass loss after an immersion time of 5 days in HBSS among the same alloy compositions, which seems to be in contradiction to the 3D synchrotron microstructural investigations for shorter immersion times. This change in the corrosion mechanism with time is attributed to the additional formation of a chemically complex corrosion product layer revealed by SEM-EDS. The observed formation of a phosphorus-rich top layer followed by a carbon-rich and oxygen-rich layer may result in speed-limiting corrosion reactions, which will in addition change the local electrolytic composition and pH conditions. This likely contributes to the low corrosion rate observed for ZX11, as well as to the accelerated corrosion rates of ZX41 and ZX21 for longer immersion times.

5. Conclusion

The analysis of the chemistry and the 3D microstructural architecture and their influence on the corrosion mechanism of

low-alloyed biodegradable Mg–Ca–Zn alloys was studied by SR- μ CT after quasi in situ immersion in HBSS for short times. The results can be summarized as follows: 1) The 3D visualization and the slices through the microstructural architecture of as-cast ZX11, ZX21, and ZX41 revealed for the first time the formation of 3D continuous interconnected networks of coexisting secondary phases, namely, $(\text{Mg}, \text{Zn})_2\text{Ca}$ and $\text{Ca}_3\text{Mg}_x\text{Zn}_{15-x}$, $4.6 \leq x \leq 12$. 2) The formation of the highest volume fraction of $(\text{Mg}, \text{Zn})_2\text{Ca}$ was observed for ZX11 compared to ZX21 and ZX41. This is assumed to relate to the mixing enthalpy among Zn, Ca, and Mg. A change in the 3D morphology by a significant growth of the secondary phases and the formation of a partially increased interface between the primary $\alpha\text{-Mg}_{\text{SS}}$ and the $(\text{Mg}, \text{Zn})_2\text{Ca}$ phase were observed for ZX41 compared to ZX21. This accelerated growth is assumed to be driven by the preferred diffusion of Ca in Mg. 3) The SR- μ CT investigations of ZX11 revealed the strongest localized corrosion attack as well as the formation of a thick and voluminous corrosion product layer after 24 h quasi in situ immersion time in HBSS compared to ZX21 and ZX41. This is associated with the high volume fraction of the less noble $(\text{Mg}, \text{Zn})_2\text{Ca}$ phase compared to $\alpha\text{-Mg}_{\text{SS}}$ and $\text{Ca}_3\text{Mg}_x\text{Zn}_{15-x}$, $4.6 \leq x \leq 12$, which leads to strong heterogeneous corrosion reactions. 4) No significant formation of a corrosion product layer and a more uniform heterogeneous corrosion process was observed for ZX21 compared to ZX41. It is concluded that the heterogeneous corrosion process of ZX21 depends strongly on the smaller size, more homogeneous distribution, and thinner morphology of the $(\text{Mg}, \text{Zn})_2\text{Ca}$ phase influencing the relative fractions of interfaces between the binary phase, the $\alpha\text{-Mg}_{\text{SS}}$, and the morphology of the ternary phase. 5) The accelerated uniformly distributed heterogeneous corrosion reactions for ZX41 compared to ZX21 are dependent on the higher volume phase fraction and of the continuous $\text{Ca}_3\text{Mg}_x\text{Zn}_{15-x}$, $4.6 \leq x \leq 12$, network, partially coexisting with the $(\text{Mg}, \text{Zn})_2\text{Ca}$ phase. Additional locally distributed heterogeneous corrosion reactions are associated with the additional formation of cone-like interfaces between $(\text{Mg}, \text{Zn})_2\text{Ca}$ and $\alpha\text{-Mg}_{\text{SS}}$.

Acknowledgements

The authors acknowledge DESY and Helmholtz-Zentrum Geesthacht for the support and provision of beamtime at the P05 beamline. The authors acknowledge the Julius Wolff Institute, Charité – Universitätsmedizin Berlin, for providing resources for data processing. The authors would also like to thank M. Thönnißen for technical support on the 2D SEM investigations.

Open access funding enabled and organized by Projekt DEAL.

Conflict of Interest

The authors declare no conflict of interest.

Data Availability Statement

Research data are not shared.

Keywords

biodegradable, biomaterials, corrosion, Mg–Ca–Zn, synchrotron microtomography, 3D microstructures

Received: February 5, 2021

Revised: April 20, 2021

Published online: June 30, 2021

- [1] M. P. Staiger, A. M. Pietak, J. Huadmai, G. Dias, *Biomaterials* **2006**, 27, 1728.
- [2] F. Witte, *Acta Biomater.* **2010**, 6, 1680.
- [3] B. J. C. Luthringer, F. Frank, W.-R. Regine, *Magnes. Res.* **2014**, 27, 142.
- [4] Y. Chen, Z. Xu, C. Smith, J. Sankar, *Acta Biomater.* **2014**, 10, 4561.
- [5] Y. Xia, B. Zhang, Y. Wang, M. Qian, L. Geng, *Mater. Sci. Eng. C* **2012**, 32, 665.
- [6] S. Zhang, X. Zhang, C. Zhao, J. Li, Y. Song, C. Xie, H. Tao, Y. Zhang, Y. He, Y. Jiang, Y. Bian, *Acta Biomater.* **2010**, 6, 626.
- [7] G. Wu, Y. Fan, H. Gao, C. Zhai, Y. P. Zhu, *Mater. Sci. Eng. A* **2005**, 408, 255.
- [8] C. J. Boehlert, K. Knittel, *Mater. Sci. Eng. A* **2006**, 417, 315.
- [9] J. Reifennrath, D. Bormann, A. Meyer-Lindenberg, in *Magnesium Alloys as Promising Degradable Implant Materials in Orthopaedic Research*, Rijeka **2011**.
- [10] Z. Li, X. Gu, S. Lou, Y. Zheng, *Biomaterials* **2008**, 29, 1329.
- [11] D. Zander, N. A. Zumnick, *Corros. Sci.* **2015**, 93, 222.
- [12] S. Jafari, R. K. S. Raman, C. H. J. Davies, J. Hofstetter, P. J. Uggowitzer, J. F. Löffler, *J. Mech. Behav. Biomed. Mater.* **2017**, 65, 634.
- [13] D. Liu, C. Guo, L. Chai, V. R. Sherman, X. Qin, Y. Ding, M. A. Meyers, *Mater. Sci. Eng. B* **2015**, 195, 50.
- [14] A. C. Hänzi, A. S. Sologubenko, P. Gunde, M. Schinhammer, P. J. Uggowitzer, *Philos. Mag. Lett.* **2012**, 92, 417.
- [15] Y. Sun, B. Zhang, Y. Wang, L. Geng, X. Jiao, *Mater. Des.* **2012**, 34, 58.
- [16] Y.-N. Zhang, D. Kevorkov, J. Li, E. Essadiqi, M. Medraj, *Intermetallics* **2010**, 18, 2404.
- [17] J. C. Gao, S. Wu, Y. Wang, L. Y. Qiao, *Mater. Sci. Forum* **2009**, 610–613, 942.
- [18] S. Cai, T. Lei, N. Li, F. Feng, *Mater. Sci. Eng. C* **2012**, 32, 2570.
- [19] P.-R. Cha, H.-S. Han, G.-F. Yang, Y.-C. Kim, K.-H. Hong, S.-C. Lee, J.-Y. Jung, J.-P. Ahn, Y.-Y. Kim, S.-Y. Cho, J. Y. Byun, K.-S. Lee, S.-J. Yang, H.-K. Seok, *Sci. Rep.* **2013**, 3, 2367.
- [20] M. Cihova, E. Martinelli, P. Schmutz, A. Myrissa, R. Schäublin, A. M. Weinberg, P. J. Uggowitzer, J. F. Löffler, *Acta Biomater.* **2019**, 100, 398.
- [21] D. Tolnai, C. L. Mendis, A. Stark, G. Szakács, B. Wiese, K. U. Kainer, N. Hort, in *In Situ Synchrotron Diffraction of the Solidification of Mg-RE Alloys* (Eds: N. Hort, S. N. Mathaudhu, N. R. Neelameggham, M. Alderman), Springer International Publishing, Cham, Switzerland, **2013**, p. 253.
- [22] S. Shuai, E. Guo, J. Wang, A. B. Phillion, T. Jing, Z. Ren, P. D. Lee, *Acta Mater.* **2018**, 156, 287.
- [23] F. Witte, J. Fischer, J. Nellesen, H.-A. Crostack, V. Kaese, A. Pisch, F. Beckmann, H. Windhagen, *Biomaterials* **2006**, 27, 1013.
- [24] J. Hofstetter, E. Martinelli, S. Pogatscher, P. Schmutz, E. Povoden-Karadeniz, A. M. Weinberg, P. J. Uggowitzer, J. F. Löffler, *Acta Biomater.* **2015**, 23, 347.
- [25] T. Kraus, S. Fischerauer, S. Treichler, E. Martinelli, J. Eichler, A. Myrissa, S. Zötsch, P. J. Uggowitzer, J. F. Löffler, A. M. Weinberg, *Acta Biomater.* **2018**, 66, 109.
- [26] A. H. Martinez Sanchez, B. J. Luthringer, F. Feyerabend, R. Willumeit, *Acta Biomater.* **2015**, 13, 16.
- [27] N. G. Grün, P. Holweg, S. Tangl, J. Eichler, L. Berger, J. J. P. van den Beucken, J. F. Löffler, T. Klestil, A. M. Weinberg, *Acta Biomater.* **2018**, 78, 378.
- [28] J. H. Hanks, R. E. Wallace, *Proc. Soc. Exp. Biol. Med.* **1949**, 71, 196.
- [29] R. Dulbecco, M. Vogt, *J. Exp. Med.* **1954**, 99, 167.
- [30] I. Greving, F. Wilde, M. Ogurreck, J. Herzen, J. U. Hammel, A. Hipp, F. Friedrich, L. Lottermoser, T. Dose, H. Burmester, M. Müller, F. Beckmann, in *SPIE – Developments in X-Ray Tomography IX*, 9212 (Ed.: R. S. Stuart), San Diego, CA, **2014**, pp. 921200.
- [31] A. Haibel, M. Ogurreck, F. Beckmann, T. Dose, F. Wilde, J. Herzen, M. Müller, A. Schreyer, V. Nazmov, M. Simon, A. Last, J. Mohr, in *Proc. SPIE*, 7804, SPIE, San Diego **2010**.
- [32] F. Wilde, M. Ogurreck, I. Greving, J. U. Hammel, F. Beckmann, A. Hipp, L. Lottermoser, I. Khokhriakov, P. Lytaev, T. Dose, H. Burmester, M. Müller, A. Schreyer, *AIP Conf. Proc.* **2016**, 1741, 030035.
- [33] D. Zander, V. F. Chaineux, N. A. Zumnick, C. Ptock, A. Kopp, in *Magnesium Alloys and Their Applications* (Eds: Z. Fan, C. Mendis), Brunel University, Beaumont Estate, Old Windsor, UK, **2018**, p. 389.
- [34] D. Zander, V. F. Chaineux, N. A. Zumnick, C. Ptock, A. Kopp, in *10th Biometal Symp. on Biodegradable Metals for Biomedical Applications*, University of Oxford, Oxford, UK, **2018**.
- [35] N. A. Zumnick, Ph.D. Thesis, RWTH Aachen University, **2018**.
- [36] E. Zhang, L. Yang, *Mater. Sci. Eng. A* **2008**, 497, 111.
- [37] H.-X. Li, S.-K. Qin, Y.-Z. Ma, J. Wang, Y.-J. Liu, J.-S. Zhang, *Int. J. Miner. Metal. Mater.* **2018**, 25, 800.
- [38] C. M. Liu, X. R. Zhu, H. T. Zhou, *Phase Diagrams of Magnesium Alloys*, Central South University Press, Changsha, **2006**.
- [39] T. V. Larionova, W.-W. Park, B.-S. You, *Scr. Mater.* **2001**, 45, 7.
- [40] J. Clark, *Trans. AIME* **1961**, 221, 644.
- [41] P. M. Jardim, G. Solórzano, J. B. V. Sande, *Microsc. Microanal.* **2002**, 8, 487.
- [42] Y.-N. Zhang, D. Kevorkov, F. Bridier, M. Medraj, *Sci. Technol. Adv. Mater.* **2011**, 12, 025003.
- [43] J. D. Cao, T. Weber, R. Schäublin, J. F. Löffler, *J. Mater. Res.* **2016**, 31, 2147.
- [44] Y. N. Zhang, D. Kevorkov, F. Bridier, M. Medraj, *Adv. Mater. Res.* **2012**, 409, 387.
- [45] A. Takeuchi, A. Inoue, *Mater. Trans.* **2005**, 46, 2817.
- [46] G. Levi, S. Avraham, A. Zilberov, M. Bamberger, *Acta Mater.* **2006**, 54, 523.
- [47] Y. Lu, A. R. Bradshaw, Y. L. Chiu, I. P. Jones, *Mater. Sci. Eng. C* **2015**, 48, 480.
- [48] M. Cihova, P. Schmutz, R. Schäublin, J. F. Löffler, *Adv. Mater.* **2019**, 31, 1903080.